



Microwave synthesis of $Y_2O_3:Eu^{3+}$ nanophosphors: A study on the influence of dopant concentration and calcination temperature on structural and photoluminescence properties



Adrine Malek Khachatourian^{a,b}, Farhad Golestani-Fard^b, Hossein Sarpoolaky^b, Carmen Vogt^c, Elena Vasileva^a, Mounir Mensi^a, Sergei Popov^a, Muhammet S. Toprak^{a,*}

^a Department of Materials and Nano Physics, KTH – Royal Institute of Technology, 16440 Kista, Stockholm, Sweden

^b School of Metallurgy and Materials Engineering, IUST – Iran University of Science and Technology, 16846 Tehran, Iran

^c Department of Biomedical and X-ray Physics, KTH – Royal Institute of Technology, 10044 Stockholm, Sweden

ARTICLE INFO

Article history:

Received 13 May 2015

Received in revised form

16 August 2015

Accepted 20 August 2015

Available online 8 September 2015

Keywords:

Phosphors

Rare earth compounds

Chemical synthesis

Luminescence

Microstructure

Optical properties

ABSTRACT

Red fluorescent emitting monodispersed spherical Y_2O_3 nanophosphors with different Eu^{3+} doping concentrations (0–13 mol%) are synthesized by a novel microwave assisted urea precipitation, which is recognized as a green, fast and reproducible synthesis method. The effect of Eu^{3+} doping and calcination temperature on the structural characteristics and luminescence properties of particles is investigated in detail. The as prepared powders have $(Y,Eu)(OH)(CO_3)$ structure which converts to $Y_2O_3:Eu^{3+}$ from 500 °C and become crystalline at higher temperatures. The crystallite size of nanophosphors increased from 15 nm to 25 nm as the calcination temperature increased from 700 °C to 1050 °C. The efficient incorporation of Eu^{3+} ions in cubic Y_2O_3 host matrix is confirmed by the calculated X-ray Powder diffraction (XRPD) structural parameters. The scanning electron microscopy (SEM) and transmission electron microscopy (TEM) micrographs show that the as obtained and calcined particles are spherical, monodispersed and non-agglomerated. The overall size of particles increases from 61 ± 8 nm to 86 ± 9 nm by increasing Eu^{3+} concentration from 0 mol% to 13 mol%. High resolution TEM revealed polycrystalline nature of calcined particles. The particles exhibit a strong red emission under ultraviolet (UV) excitation. The photoluminescence (PL) intensity of the peaks increases proportionally with Eu^{3+} concentration and the calcination temperature with no luminescence quenching phenomenon observed even for $Y_2O_3:13\%Eu^{3+}$. The fluorescent emission properties combined with the monodispersity and narrow size distribution characteristics make the $Y_2O_3:Eu^{3+}$ heavy metal free nanophosphors applicable in fluorescence cell imaging and as fluorescence biolabels.

© 2015 Elsevier B.V. All rights reserved.

1. Introduction

The bioimaging applications of quantum dots (QDs) are a well-established and still expanding research field. Although Cd based QDs are dominating the area, their inherent toxicity pose a limitation reflected in their application mainly in in-vitro research. There is a continuing quest for new materials with similar or better properties than the heavy metal based QDs. Rare earth (Re^{3+}) doped inorganic nanoparticles are extensively used in high performance luminescence devices, catalysts, magnets and other functional materials due to their unique optical, chemical, and electronic properties originating from the doping element 4f electrons [1]. The intense fluorescent emission, excellent stability

and potential low toxicity make the Re^{3+} doped inorganic nanoparticles promising phosphors for applications in bio-related area such as fluorescence cell imaging or fluorescence biolabels [2].

Oxide host compounds are nontoxic and environmental friendly and consequently are preferred. Yttrium oxide (Y_2O_3) has a body centered cubic structure and particularly is an excellent host material when trivalent lanthanide ions are used as dopants. It is preferred due to matching of its ionic radius with the dopant ions and similar chemical properties [3]. Furthermore, in comparison with other oxide materials, Y_2O_3 have high chemical and thermal stability and a broad transparency region [4]. Additionally, the wide band gap (5.8 eV) of Y_2O_3 decreases the effect of optical absorption by the host and the small phonon energy (380 cm^{-1}) of this material increases the possibility of the radiative transitions between electronic energy levels of the rare earth ions in the host [5].

* Corresponding author. Tel.: +46 8 7908344; fax: +46 8 7505173.

E-mail address: toprak@kth.se (M.S. Toprak).

The luminescence mechanism of inorganic $Y_2O_3:Re^{3+}$ phosphors is different from semiconductor QDs. QDs are nanometers sized crystalline semiconductor clusters (1–10 nm). At nanometer scale the quantum confinement effect gives rise to unique optical and electronic properties, which are size and morphology dependent. The energy of the band gap in a QD determines the wavelength range of absorbed and emitted light, which decreases with decreasing size of QDs [6,7]. Comparatively, in $Y_2O_3:Re^{3+}$ system the emission wavelength of each dopant is independent of the particle size and depends only on the dopant ion [8]. Each dopant atoms create their own atomic levels within the band gap of the host material and show abundant emission colors due to their 4f–4f or 5d–4f transitions. This allows a large flexibility in synthesizing particles with sizes tuned by their final applications. The emission colors of Y_2O_3 doped with Eu^{3+} , Tb^{3+} , Tm^{3+} or Dy^{3+} ions are red, green, blue, and yellow respectively [9]. Different colors can be obtained by using multiple dopants in the same matrix and by adjusting the ratios between the dopants [10,11].

$Y_2O_3:Eu^{3+}$ is an important red emitting phosphor widely used in fluorescent lamps and display devices such as plasma display panel (PDP) and field emission display (FED). It has excellent luminescence properties such as high quantum efficiency, color purity, high brightness, and good atmospheric stability [12,13]. New applications in biomedical related areas are emerging for $Y_2O_3:Eu^{3+}$ materials due to their inherent nontoxicity. Moreover, properties as photostability, biocompatibility, sharp emission and absorption bands and long life time make $Y_2O_3:Eu^{3+}$ suitable for biomolecular detection as bioimaging probes or biolabels [14].

The synthesis methods and the study of luminescence properties of $Y_2O_3:Re^{3+}$ nanocrystals are an active field of research. Solid state synthesis method is a conventional method used for producing ceramics, including $Y_2O_3:Eu^{3+}$ phosphors, which requires high temperatures (1300–1500 °C) and prolonged calcination time. This method results in particles that are micrometer size, agglomerated and display irregular morphology, which requires grinding or milling to obtain finer powders. The luminescence efficiency of the phosphors greatly decreases in this process [15,16]. Additionally, most of the wet chemistry synthesis methods like sol–gel route [17], combustion synthesis [18], hydrothermal process [19], solvothermal technique [20] or microemulsion method [21] are relatively complicated and demand high-temperature, high-pressure, or long-time treatments. Furthermore, the obtained particles by many of these methods are agglomerated, irregular in shape and size. For good luminescent characteristics particles must have a crystalline structure, have to be monodisperse with a spherical morphology. In displays applications all these desired properties will result in higher screen resolution, high packing density and reduced light scattering [22]. For bioimaging application the narrow size distribution and the size of less than a few hundred nanometers are highly recommended [23]. Optimizing the existing methods for synthesizing $Y_2O_3:Re^{3+}$ nanocrystals with controllable size, narrow size distribution and spherical shape is attracting a lot of interest.

Microwave method is a green, fast, surfactant and hazardous precursors free and large-scale reproducible synthesis method. The main characteristic of the method is the uniform heating of the solution within few minutes due to rapid kinetics of the dipole moments of the component molecules in the field of oscillating electromagnetic radiations [24,25]. In our earlier work [26], Y_2O_3 nanocrystals were synthesized by an optimized microwave assisted urea precipitation method. The effects of reaction parameters such as metal ions and urea concentration, reaction temperature and reaction time on the obtained particles have been investigated. In this paper the optimized parameters of microwave

assisted urea precipitation method are used for the synthesis of monodispersed spherical $Y_2O_3:Eu^{3+}$ red emitting nanocrystals with different doping concentration (1–13 mol%). Additionally, the effect of Eu^{3+} doping and calcination temperature on structural and luminescence properties and also on the particle size is investigated in details.

2. Experimental

2.1. Materials and methods

Yttrium nitrate hexahydrate, $Y(NO_3)_3 \cdot 6H_2O$ (Sigma-Aldrich 99.98%), europium nitrate pentahydrate, $Eu(NO_3)_3 \cdot 5H_2O$ (Sigma-Aldrich 99.99%) and urea (Merck $\geq 99\%$) were used as received, without further purification.

Microwave assisted urea precipitation technique is used to synthesize spherical $Y_2O_3:Eu^{3+}$ nanocrystalline particles. The details of the method are given elsewhere [26]. Typically, $Y(NO_3)_3 \cdot 6H_2O$, $Eu(NO_3)_3 \cdot 5H_2O$, and urea are dissolved separately in deionized (DI) water (Millipore, 15 M Ω cm) to prepare stock solutions of $Y(NO_3)_3$, $Eu(NO_3)_3$ and urea respectively. Solutions with fixed concentration of metals ions [$Y^{3+} + Eu^{3+}$]=0.005 M and [urea]=0.25 M are prepared, while [Eu^{3+}] is varied from 1 to 13 (1, 3, 5, 9 and 13) mol%. The solutions are subsequently heated in a Biotage[®] initiator classic laboratory microwave (Biotage, Sweden), oven at 2.45 GHz radiation frequency, under magnetic stirring (600 rpm) for 10 min at 90 °C. The resulting precipitates are collected by centrifugation (8000 rpm), washed with DI water and ethanol (Solveco 99.5%) and dried at 60 °C overnight. Further calcination of the powders is performed in air at various temperatures ranging from 300 °C to 1050 °C for 2 h.

2.2. Characterizations

PAN analytical X'Pert Pro powder diffractometer (Cu-K $\alpha_{1,2}$ radiation, 45 kV, 35 mA) is used for phase identification. Data is collected at every 0.01° in angle range 10–90° in 2 θ . The counting time is fixed to 40 s at every step. The 1/8° fixed divergence slit and 1/4° fixed anti-scatter slit are used without presence of secondary monochromator. Fourier Transform Infrared Spectroscopy (FT-IR) analysis of powders is performed using Nicolet iS10 spectrophotometer (Thermo scientific, USA). Thermogravimetric analysis (TGA) is done in synthetic air atmosphere in the temperature range of 20–1000 °C with a heating rate of 10 °C/min using TGA-Q500 (TA instruments, USA). The Photoluminescence (PL) emission and excitation spectra are performed using Perkin-Elmer LS 55 fluorescence spectrometer (Perkin Elmer, USA). The same concentration of powders are dispersed in deionized water in order to compare the PL emission and excitation intensity of samples with different Eu^{3+} concentrations or different calcination temperatures. The absorption spectra is measured using Perkin Elmer Lambda 750 UV–vis spectrometer (Perkin Elmer, USA).

The fluorescence images of the Y_2O_3 particles doped with (5 mol%) Eu^{3+} are obtained. The diluted solution of the doped particles is placed on a plastic tape by drop casting technique. The powders are pumped by third harmonic generation (THG) of solid state Ti:Al₂O₃ laser (Coherent Chameleon, Coherent, UK). The pulses have 705 nm wavelength, 80 MHz pulse repetition rate, 140 fs pulse duration and the final excitation wavelength is 235 nm. To suppress blue light from the tape and glass substrate, the pump power level is adjusted to 300–350 μ W. A charge-coupled device (CCD) camera (Discovery VMS-004 Deluxe USB Microscope, VEHO, USA) is used for fluorescence imaging.

Zeiss Ultra 55 FEG-SEM Scanning electron microscopy (SEM) (Zeiss, Germany) equipped with an energy dispersive X-ray

spectroscopy (EDS) is used for microstructure characterization and elemental mapping of the calcined powders. JEOL JEM-2100F field emission transmission electron microscopy (TEM) operating at an accelerating voltage of 200 kV (JEOL Ltd., Japan) is used for the size and morphology characterizations of as prepared and calcined powders. The powders are dispersed in ethanol, sonicated for 1 min, dropped onto a carbon coated TEM grid and are allowed to dry at room temperature overnight. The mean size diameter and standard deviation (SD) is calculated from at least 300 particles from different TEM micrographs. Additionally, the selected area electron diffraction (SAED) patterns are obtained.

3. Results and discussion

3.1. Structural analysis

3.1.1. X-ray Powder diffraction (XRPD)

The crystalline phase of particles doped with different concentrations of Eu (0–13 mol%) and subsequently calcined at 900 °C for 2 h is characterised by XRPD (Fig. 1a). All diffraction peaks can be indexed to Y_2O_3 that crystallize in cubic space group $la3$ (206). (JCPDS: 01-073-1334). No impurity phases or unreacted constituents can be detected and the structure of cubic phase of Y_2O_3 is not affected by presence of dopant ion (Eu^{3+}). The particles are well crystallized and notably no additional peaks corresponding to Europium or Eu_2O_3 appear even for the highest Eu^{3+} content $Y_2O_3:13\%Eu^{3+}$.

Structural parameters of $Y_2O_3:Eu^{3+}$ powders calculated from XRPD datas are shown in Table 1. The lattice constant (a) of the powders and the particle density (D_x) are calculated according to Eqs. (1) and (2) respectively.

$$\frac{1}{d^2} = \frac{h^2 + k^2 + l^2}{a^2} \quad (1)$$

$$D_x = \frac{16M}{(N_A \cdot a^3)} \quad (2)$$

where M is the molecular weight, N_A is the Avogadro's number and a^3 is volume of the unit cell. Five main peaks with Miller indices (2 1 1), (2 2 2), (4 0 0), (4 4 0), and (6 2 2) are used for lattice constant calculations. Increasing the concentration of the Eu^{3+} from 0% to 13%, the peaks in the XRPD patterns are shifting towards lower 2θ angles, for example for (2 2 2) plane from 29.09° (Eu^{3+} 0%) to 29.00° (Eu^{3+} 13%). Due to this shift the calculated lattice constant (a) of Y_2O_3 increases from 10.622 ± 0.013 (Eu^{3+} 0%) to 10.654 ± 0.013 (Eu^{3+} 13%) and consequently causes the

decrease in particles density (D_x) from 5.00 g/cm³ (Eu^{3+} 0%) to 4.96 g/cm³ (Eu^{3+} 13%). Additionally, the lower degree shift in the position of the diffraction peaks confirms the substitution of the Eu^{3+} ion in the host lattice, knowing that the ionic radius of Eu^{3+} (0.109 nm) is larger than that of Y^{3+} (0.104 nm) [5]. The doping with Europium ions from 0 mol% to 13 mol% results in a linear increase of the lattice constant (Fig. S1). The linear function $a = a_0 + b_0x$ ($a_0 = 10.62277 \pm 0.00056$, $b_0 = 0.00247 \pm 0.00008$) is used to fit the relationship between unit-cell parameter and concentration. The observed linearity means that Vegard's rule is obeyed and also confirms the formation of the substitutional solid solution $Y_{2-x}Eu_xO_3$. The same behavior for $Y_{2-x}Yb_xO_3$ nanoparticles synthesized by thermal degradation method is reported by Antic et al. [27].

The crystallite size of the samples is calculated using the Scherrer equation using the strongest peak of (2 2 2) plane (Eq. (3)) [28]

$$D = \frac{k \lambda}{\beta \cos \theta} \quad (3)$$

where D is the crystallite size, K is a constant ($K=0.89$), λ is the X-ray wavelength ($\lambda=0.15405$ nm), θ is the diffraction angle (degree), and β is full-width at half-maximum (FWHM, in radian) of an observed peak. The calculated crystallite size of ~19 nm is not varying significantly with the dopant concentration (Table 1). The same phenomena was observed by Mayrinck et al. [29] where the crystallite size of the Y_2O_3 particles doped with Eu^{3+} was reported to be relatively independent of the doping ion concentration.

It has been shown that the full-width at half-maximum (FWHM), the β , of an observed peak can be influenced by a combination of crystallite size and lattice strain. The effect of the crystallite size and effective strain can be expressed by the Williamson–Hall equation (Eq. (4)) [28].

$$\beta \cos \theta = \frac{k\lambda}{D} + 4\epsilon \sin \theta \quad (4)$$

The effective strain (ϵ) is determined from the slope of the plot $\beta \cos \theta$ (y -axis) versus $4 \sin \theta$ (x -axis) and the effective crystallite size (D) from the intercept $\frac{k\lambda}{D}$ on the y -axis (Williamson–Hall plot). Five main peaks with Miller indices (2 1 1), (2 2 2), (4 0 0), (4 4 0), and (6 2 2) are used for Williamson–Hall plot. The results from the calculations are summarized in Table 1 and the corresponding Williamson–Hall plot are presented in Fig. S2. For example, Fig. S2 (b) represents the Williamson–Hall plot of $Y_2O_3:1\%Eu^{3+}$ particles, depicting a linear dependence with the slope of the fitting resulting in a lattice strain (ϵ) of 2.7×10^{-4} . The calculated

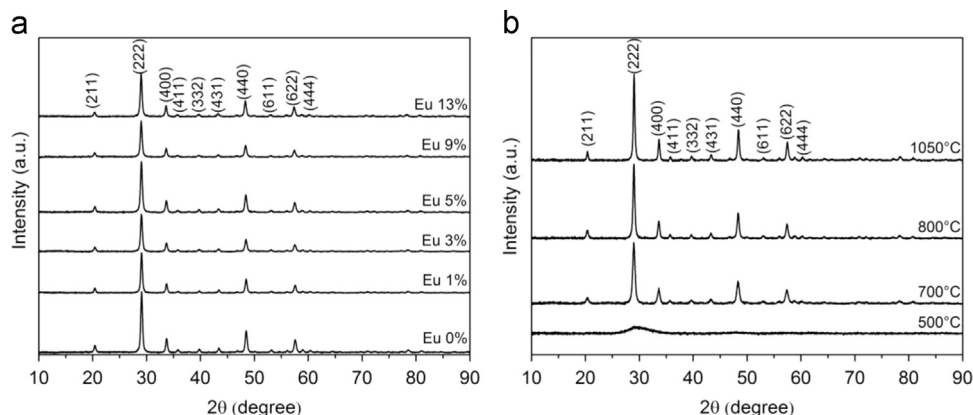


Fig. 1. XRPD patterns of (a) Y_2O_3 powders doped with different Eu^{3+} concentrations (0–13 mol%) after calcination at 900 °C for 2 h and (b) XRPD patterns of $Y_2O_3:9\%Eu^{3+}$ powders calcined at different temperatures (from 500 °C to 1050 °C) for 2 h.

crystallite size with two different methods has similar values. The strain is increased in the doped samples compared to pure Y_2O_3 probably due to the fact that Eu^{3+} ion have a much larger ionic radius than Y^{3+} . Therefore, substitution of Eu^{3+} into Y^{3+} lattice sites leads to a much higher distortion of the periodic lattice of the host. This is confirmed by the larger lattice constant of $Y_2O_3:Eu^{3+}$ nanoparticles compared with the Y_2O_3 lattice constant values (Table 1). Further, higher strain values might result in the decrease of the emission intensity. However, the calculated strain values in the doped samples are very small ($\sim 10^{-4}$) which reflects the negligible effect of the doping ions in the strain even at high doping concentration (Eu 13%).

In order to study the effect of calcination temperature on crystal structure of $Y_2O_3:Eu^{3+}$ powders, the $Y_2O_3:9\%Eu^{3+}$ powders were calcined at different temperatures (500–1050 °C) for 2 h and analyzed by XRPD. The powders calcined at 500 °C had Y_2O_3 phase with low crystallinity (Fig. 1b). Increasing the calcination temperature results in stronger and sharper peaks due to improved crystallinity of the samples. The enhanced crystallinity is confirmed by a decrease of the calculated lattice constant and consequently causes the increase in particles density. The lattice constant of $Y_2O_3:9\%Eu^{3+}$ powders is changing from 10.655 ± 0.013 Å (700 °C) to 10.640 ± 0.013 Å (1050 °C) which is closer to the theoretical value of pure Y_2O_3 of 10.604 Å. The increase of the calcination temperature also leads to an increase in the calculated crystallite size (Scherrer equation) from 14.7 nm at 700 °C to 22.3 nm at 1050 °C (Table S1). Similar values are obtained from Williamson–Hall plot. The direct dependency between the calcination temperature and the crystallite size was previously reported in the literature [5,20,22,29–31] and is attributed to growth of the crystals at higher temperatures [32]. Furthermore, the Williamson–Hall plot of the samples calculated from XRPD data are represented in Fig. S3. Similar values with the ones obtained from the Scherrer method for the crystallite size are extracted from Williamson–Hall plot. Although the fitting is linear

and the best fit is obtained increasing the calcination temperature, we donot observe a decrease of the lattice strain with the increase in calcination temperature as previously reported [33,34]. Our results are probably due to the different synthesis method used in the present study compared with the ones from the cited literature (microwave assisted method vs combustion or sol gel method). Additionally, the microstructure of the obtained particles in this study (polycrystallites embedded in less than ~ 100 nm particles) is different from single crystals particles architecture in the mentioned literature [33,34].

3.1.2. Fourier Transform Infrared Spectroscopy (FT-IR)

The FTIR spectra of samples are presented in Fig. 2. For the particles calcined at 300 °C, the broad absorption band centered at ~ 3500 cm^{-1} is attributed to O–H stretching vibration while other bands are assigned to C–O vibrations in CO_3^{2-} (the bands around 1520 cm^{-1} and 1430 cm^{-1} from asymmetric stretch of C–O vibration, band at 1085 cm^{-1} from symmetric stretch of C–O vibration and the band at 850 cm^{-1} from the deformation vibration of C–O) [32,35]. With respect to the absorption band in the spectra the composition of this powder is $(Y,Eu)(OH)(CO_3)$. Increasing the calcination temperature, the absorption peaks disappear and a new peak at 560 cm^{-1} appears which can be attributed to $Y(Eu)$ –O stretching vibration, revealing the formation of $Y_2O_3:Eu^{3+}$ (Fig. 2a). Annealing improves the intensity of this peak due to increase in crystallinity, which is in accordance with XRPD results. The powders with different doping concentrations have very similar FTIR spectra, which reflect similar composition of the samples (Fig. 2b).

3.1.3. Thermogravimetric analysis (TGA)

Thermal stability of doped and undoped samples is analyzed by TGA (Fig. S4). Samples with 0 mol% and 5 mol% of Eu^{3+} have similar thermal behavior and the continuous weight loss from 100 °C to 850 °C is attributed to thermal decomposition of the

Table 1
Structural parameters of Y_2O_3 powders doped with different Eu^{3+} concentrations (0–13 mol %) and calcined at 900 °C for 2 h.

Eu^{3+} (mol%)	0	1	3	5	9	13
2θ position of (2 2 2) plane (deg)	29.09	29.08	29.06	29.05	29.02	29.00
FWHM (β) of (2 2 2) peak (deg)	0.42	0.40	0.44	0.45	0.44	0.43
Lattice constant (a) (Å)	10.622 ± 0.013	10.625 ± 0.013	10.631 ± 0.012	10.635 ± 0.013	10.646 ± 0.012	10.654 ± 0.013
Particle density (D_x) (g/cm ³)	5.00	5.00	4.99	4.98	4.96	4.96
Crystallite size (D) (nm) – Scherrer method	19.3	20.7	18.8	18.4	18.9	19.2
Crystallite size (D) (nm) – Williamson–Hall method	19.5	21.7	18.7	18.2	19.5	19.8
Strain (ϵ) – Williamson–Hall method (10^{-4})	0.1	2.7	1.7	2.1	2.4	1.9

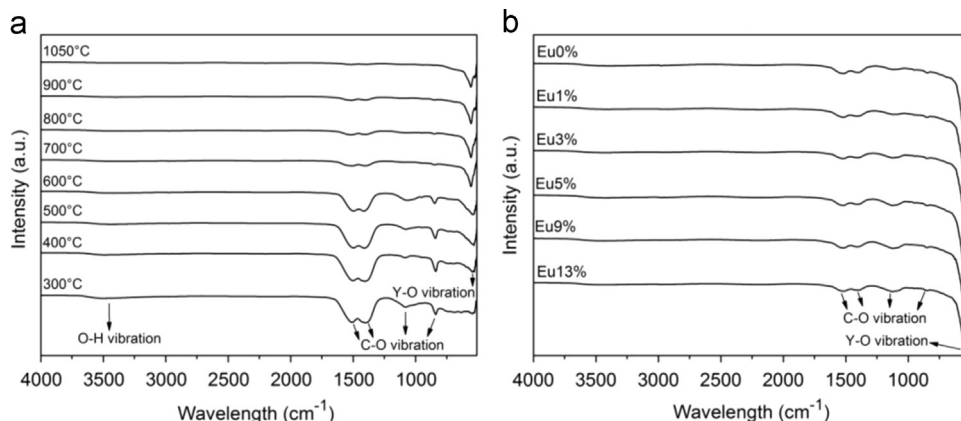


Fig. 2. FTIR spectra of (a) $Y_2O_3:9\%Eu^{3+}$ powders calcined at different temperatures (from 300 °C to 1050 °C) for 2 h, and (b) Y_2O_3 powders doped with different Eu^{3+} concentration (0–13 mol%) after calcination at 800 °C for 2 h.

hydroxycarbonate precursor. The residual weight does not change above 850 °C which confirms that $(Y,Eu)(OH)CO_3$ is totally decomposed to oxide form.

3.2. Optical properties

3.2.1. UV–vis

The UV–vis absorption spectra of Y_2O_3 powders doped with different Eu concentrations are displayed in Fig. 3. For doped and undoped powders a sharp absorption band at 210 nm is observed which is mainly due to the band gap of Y_2O_3 phosphors [36,37].

3.2.2. Emission spectra

The PL spectrum of $Y_2O_3:Eu^{3+}$ samples are recorded by UV excitation (235 nm) at room temperature (Fig. 4). The emission spectrum is composed of characteristic emission lines of Eu^{3+} ions attributed to the ${}^5D_0-{}^7F_j$ ($j=0,1,2,3,4$) transition of Eu^{3+} ion in Y_2O_3 lattice. The energy level diagram of Eu^{3+} ion in Y_2O_3 lattice explains the observed transitions (Fig. S5). Emission peaks at 582 nm (${}^5D_0-{}^7F_0$), 588 nm, 595 nm, 600 nm (${}^5D_0-{}^7F_1$), and 613 nm, 632 nm (${}^5D_0-{}^7F_2$) are assigned to the corresponding transitions, and it can be described in terms of Judd–Oflet theory [38,39].

The dependence of the PL emission intensity with the doping concentration (Fig. 4a) and calcination temperature (Fig. 4b) is investigated. The symmetry of the local environment of the Eu^{3+} ions influence the position and intensity of the emission peaks [40]. The Y_2O_3 cubic lattice has two different crystallographic cation sites with non-centrosymmetric or centrosymmetric

symmetry. 75% of these sites are non-centrosymmetric C_2 sites and the remaining 25% are centrosymmetric S_6 (C_{3i}) sites [41]. Eu^{3+} ions can occupy both symmetry sites replacing the Y^{3+} on those locations [40]. In the obtained particles the cationic distribution in Y_2O_3 matrix might differ from the theoretical value ($C_2/C_{3i}=3$) due to different factors as: synthesis method, particle/crystallite size, dopant concentration and strain. Preferably, from the optical point of view, Re^{3+} ions should occupy C_2 sites in rare earth doped based phosphors [27,42,43]. ${}^5D_0-{}^7F_0$, ${}^5D_0-{}^7F_2$, and ${}^5D_0-{}^7F_3$ transitions originate from C_2 sites by electric dipole transition and are very sensitive to the local structure and site asymmetry around Eu^{3+} . The splitting of ${}^5D_0-{}^7F_1$ transitions originates from C_2 and S_6 sites by magnetic dipole transition and are mostly independent of the local environment [5,43].

Investigating the dependence of the PL emission intensity with the doping ion concentration (Fig. 4a) we observed that the peaks intensity is varying by increasing Eu^{3+} concentration. However, the emission peaks have the same positions for samples with different doping levels. The intensity depends on the number of emitted photons [43]. In the spectra, the most intense red emission peak at 613 nm is due to the hypersensitive forced electric dipole transition of ${}^5D_0-{}^7F_2$. The 613 nm peak is attributable to the presence of Eu^{3+} that occupies a low symmetry local site in Y_2O_3 matrix and is very sensitive to environmental effects [44]. The PL intensity of this peak increases with enhancing of Eu^{3+} concentration due to higher number PL active centers (Eu^{3+} ions). The other important emission peak is orange emission at 588 nm corresponding to the magnetic dipole transition of ${}^5D_0-{}^7F_1$. The ratio between the intensity of the red emission and the orange emission peaks (R/O) is reported as a sensitive parameter to understand the variation of the local symmetry around Eu^{3+} in the lattice [33]. The R/O increases from 1.1 for $Y_2O_3:1\%Eu^{3+}$ to 8.4 for $Y_2O_3:13\%Eu^{3+}$ indicating a change in symmetry of the crystal field around Eu^{3+} (Fig. S6b). The increase of the R/O ratio with the increase of the dopant concentration is possibly due to strong energy transfer from the Eu^{3+} ions occupying the S_6 site to the Eu^{3+} ions located in C_2 site [5]. Packiyaraj et al. [5] suggested that the higher values of R/O confirm the strong covalent nature of the Eu^{3+} bonding with the surroundings. To conclude, the $Y_2O_3:13\%Eu^{3+}$ particles having the highest PL intensity of ${}^5D_0-{}^7F_2$ transition that is originating from C_2 sites is the best candidate for applications in fluorescence cell imaging and cell labeling.

The luminescence quenching mechanism with increasing the concentration of the dopant ions is previously reported. The critical quenching concentration of dopant is defined as the concentration at which the emission intensity begins to decrease while the dopant concentration is increasing [45]. In literature [35,36,46–48], the critical quenching concentration for $Y_2O_3:Eu^{3+}$

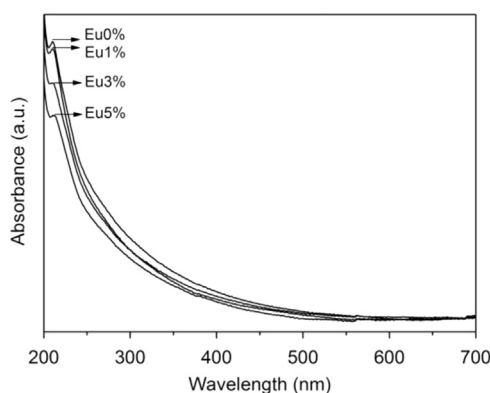


Fig. 3. UV–vis absorption spectra of Y_2O_3 powders doped with different Eu^{3+} concentrations (0–5 mol%) after calcination at 900 °C for 2 h.

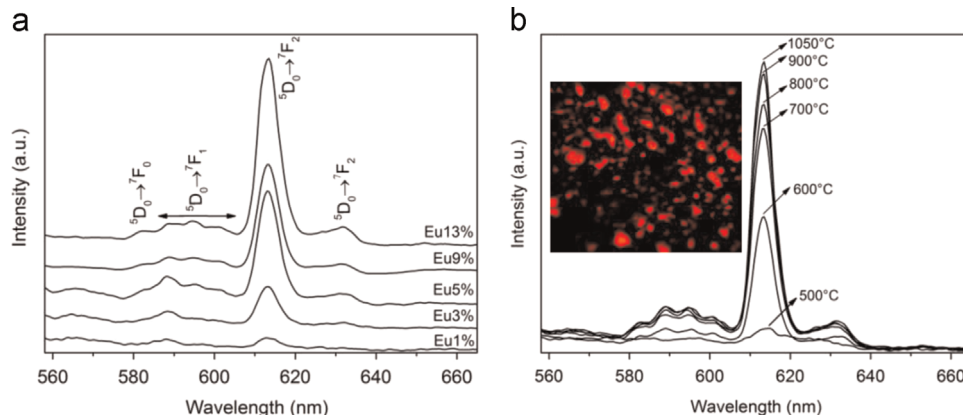


Fig. 4. PL spectra of (a) Y_2O_3 powders doped with different Eu^{3+} concentrations (1–13 mol%) calcined at 900 °C for 2 h, and (b) $Y_2O_3:9\%Eu^{3+}$ powder calcined at different temperatures (from 500 °C to 1050 °C) for 2 h. Inset in (b) shows fluorescence image of typical calcined powder of $Y_2O_3:Eu^{3+}$.

particles vary from 3 mol% to 9 mol%. The quenching concentration of Eu^{3+} is attributed to non-radiative transition of absorbed energy between neighboring Eu^{3+} ions [35,43]. The quenching phenomenon is though not observed in the present study even for 13 mol% Eu^{3+} doped samples. It is important to note that this doping ion concentration (13 mol%) is higher than other doping levels obtained with conventional methods. The higher critical quenching concentration observed for nanopowders was attributed to the nanostructure architecture of the particles by Hoe et al. [48]. The non-radiative transitions can be triggered by quenching centers (traps) distributed randomly in the particles. These traps are created by impurities or defects remained from the synthesis procedure. However, in the particles containing few or no traps, quenching occurs at higher concentration or is not present at all. In line with our observations, Antic et al. [43] reported the absence of the quenching with increasing Eu^{3+} concentration up till 10 mol% for $\text{Y}_2\text{O}_3:\text{Eu}^{3+}$ particles synthesized by thermolysis method. Overall cation distribution, dopant concentration and microstructures of powders are determining the differences in emission intensities and critical quenching concentration. The absence of the quenching in our study even at high Eu^{3+} concentration results in a better luminescence performance of these particles fabricated using the methodology described in this work.

The effect of calcination temperature on the PL emission intensity is also studied (Fig. 4b). The emission intensity for all peaks increases with the calcination temperature and the positions of the peaks are found to be unaffected. For the samples calcined at 500 °C very weak red emission at 613 nm is observed due to the low crystallinity of samples. However, annealing improves the luminescent efficiency as a result of improved crystallinity, growth in the crystallite size and removal of organic groups, which is consistent with XRPD, TGA and FTIR results. Similar observations are reported in the literature for the overall increase in the intensity with calcination temperature for powders synthesized by other methods attributed to the enhanced crystallinity of the powders [5,34,36,49] which allows a better activation for the Eu^{3+} centers [35,47]. However, Yan et al. and Murgan et al. [22,25] reported a decrease of luminescence intensity at higher calcination temperatures probably induced by agglomeration of particles. The monodispersity and the absence of agglomeration when increasing the calcination temperature in this study (see Section 3.3.) can explain the fact that we do not observe an indirect dependency between the luminescence intensity and the calcination temperature. Furthermore, the R/O is not changing significantly with calcination temperature (from 6.3 for particles calcined at 600 °C to 6.5 for particles calcined at 1050 °C) suggesting that Eu^{3+} ionic environment is not modified under

different calcination temperatures (Fig. S6d), which is in agreement with the findings of Boukerika et al. [34].

3.2.3. Excitation spectra

Excitation spectra of samples are obtained by monitoring the emission wavelength fixed at 613 nm, corresponding to ${}^5\text{D}_0\text{--}{}^7\text{F}_2$ transition (Fig. 5). The broad excitation band at ~ 235 nm is attributed to charge transfer band (CTB) of Eu^{3+} which corresponds to the electronic transition from 2p orbital of O^{2-} (valance band) to the empty 4f orbital of Eu^{3+} . In the current work no excitation peaks can be observed in the range of 300–500 nm in agreement with previous reports [39,48,50], although the presence of less intense peaks in this interval attributed to intra-configurational $4f^6\text{--}4f^6$ transitions of Eu^{3+} have been observed previously [1,20]. Additionally we observe that the intensity of the 235 nm peak increases with the increase in the doping concentration and calcination temperature (Fig. 5a and b). This is probably due to the fact that electron transition to CTB promotes under higher calcination temperatures and higher Eu^{3+} concentrations, and consequently enhanced PL emission intensity.

3.2.4. Fluorescence imaging

The fluorescence image of typical calcined powder of $\text{Y}_2\text{O}_3:\text{Eu}^{3+}$ is shown in the inset of Fig. 4b. The Eu^{3+} doped Y_2O_3 powders have red luminescence emission under UV excitation (235 nm), which is in accordance with the PL results. The red emission of the particles demonstrates that the powders have potential applications in fluorescence bio imaging.

3.3. Microstructure analysis

The morphology, size and size distribution of powders are characterized by SEM and TEM. SEM micrographs of calcined Y_2O_3 and $\text{Y}_2\text{O}_3:\text{Eu}^{3+}$ powders show the uniform spherical shape and monodispersity of powders in large scale (Fig. 6a and b). The EDS analysis reveals the desired ratio of doping has been achieved by the calculated ratio of Eu (data not shown). Elemental mapping of Y and Eu elements confirms the homogenous distribution of Eu in Y_2O_3 host structure for $\text{Y}_2\text{O}_3:\text{Eu}^{3+}$ powders (Fig. 6c and d).

Detailed microstructural analysis of as prepared and calcined particles is performed by TEM. As prepared samples are monodispersed spherical particles with narrow size distribution (Fig. 7a). Increasing the Eu^{3+} concentration, the size of the particles slightly increases from 79 ± 11 nm (Eu^{3+} 0%) to 106 ± 16 nm (Eu^{3+} 13%), (Table 2). Similar behavior is previously reported by Huang et al. for $\text{Y}_2\text{O}_3:\text{Nd}^{3+}$ particles [31]. The size of particles decreases after calcination due to phase transformation of $(\text{Y,Eu})(\text{OH})\text{CO}_3$ to $\text{Y}_2\text{O}_3:\text{Eu}^{3+}$ (Fig. S7). The size shrinkage is

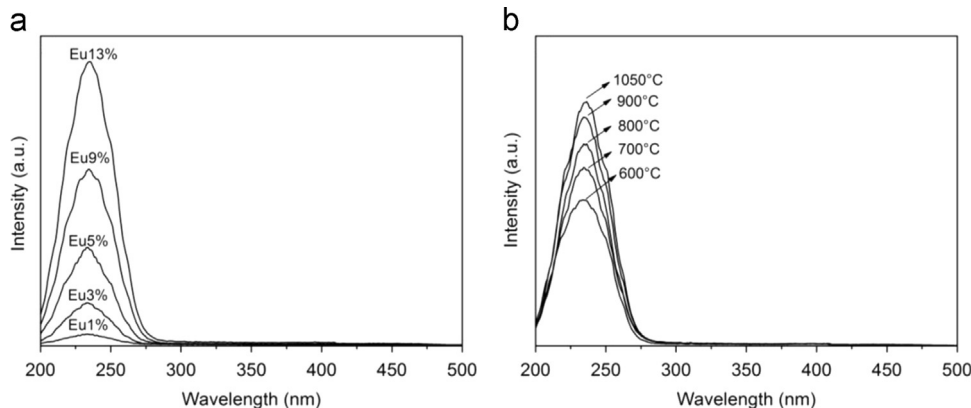


Fig. 5. Excitation spectra of (a) Y_2O_3 powders doped with different Eu^{3+} concentrations (1–13 mol%) after calcination at 900 °C for 2 h, and (b) $\text{Y}_2\text{O}_3:9\%\text{Eu}^{3+}$ powders calcined at different temperatures (from 600 °C to 1050 °C) for 2 h.

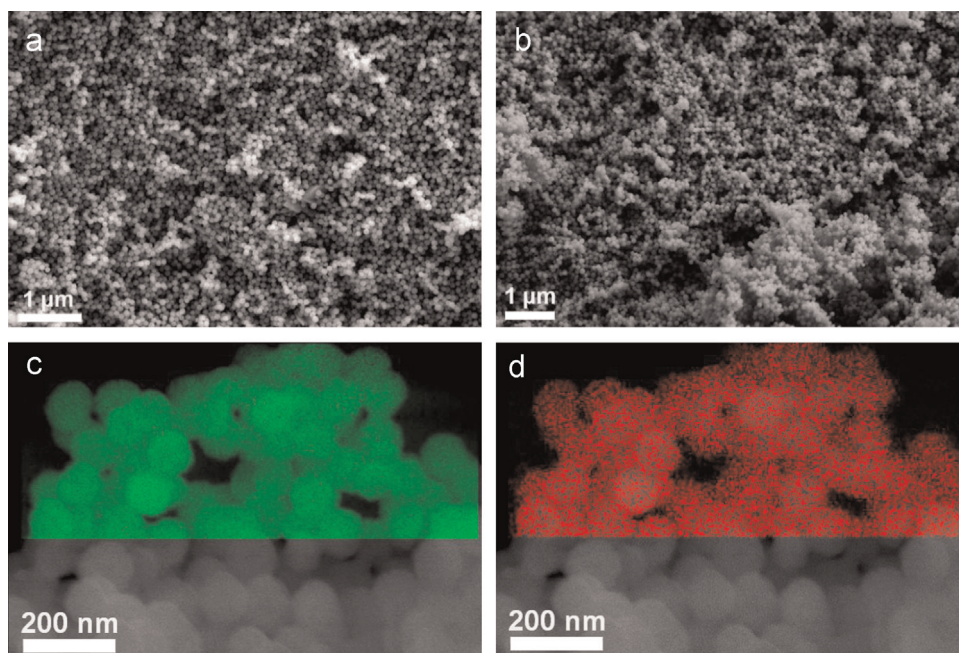


Fig. 6. SEM micrographs of (a) Y_2O_3 , (b) $\text{Y}_2\text{O}_3:13\%\text{Eu}^{3+}$ calcined at 900°C for 2 h, (c) elemental mapping of Y (green color) and (d) elemental mapping of Eu (red color). (For interpretation of the references to color in this figure legend, the reader is referred to the web version of this article.)

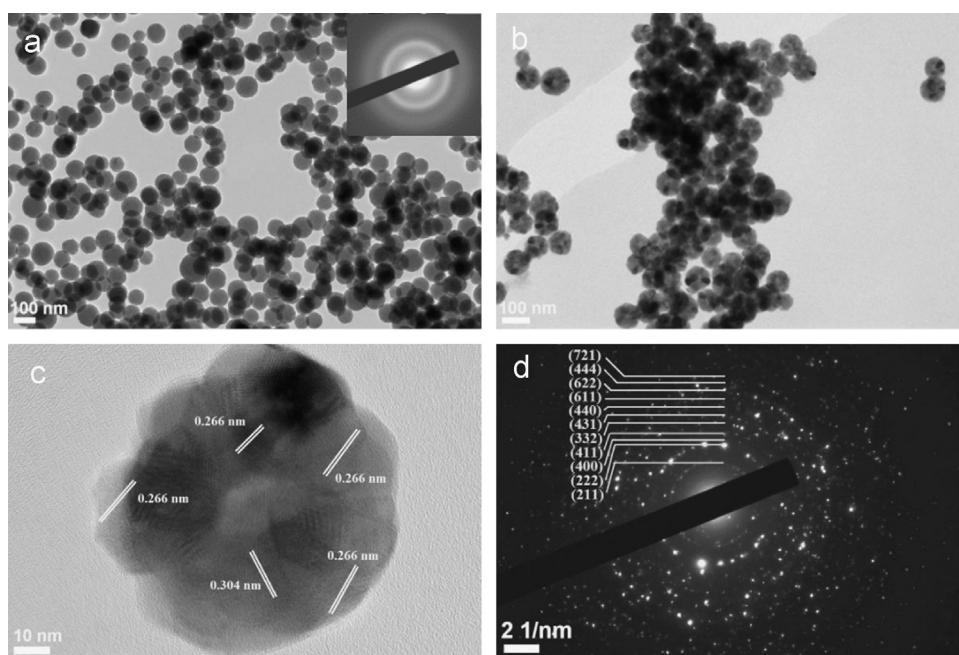


Fig. 7. TEM micrograph of $\text{Y}_2\text{O}_3:1\%\text{Eu}^{3+}$ (a) as prepared powder, (b) calcined powder at 900°C for 2 h, (c) higher magnification TEM, and (d) SAED pattern of calcined powder.

common for rare earth compounds decompositions [39]. However, the morphology of the particles is not affected by calcination and the precursor spherical shape is maintained (Fig. 7b). Higher magnification TEM confirms that the calcined particles are polycrystalline particles, consisting of smaller crystallites of $\sim 20\ \text{nm}$ for particles calcined at 900°C (Fig. 7c). The size of the crystallites is in agreement with the crystallite size calculated from XRPD patterns using the Scherrer or Williamson–Hall equations. The lattice fringes in micrograph confirm the high crystallinity of the powder. Furthermore, the lattice interplanar spacing is measured to be

Table 2

The relationship between particle size and Eu^{3+} mol% for as prepared particles, and particles calcined at 900°C for 2 h.

Eu^{3+} (mol%)	0	1	3	5	9	13
Particle size – as prepared powders (nm)	79 ± 11	79 ± 12	86 ± 17	89 ± 12	88 ± 16	106 ± 16
Particle size – calcined powders (nm)	61 ± 8	60 ± 7	69 ± 11	71 ± 10	73 ± 13	86 ± 9

0.304 nm and 0.266 nm corresponding to the (2 2 2), and (4 0 0) planes of cubic Y_2O_3 respectively.

The SAED pattern for the as prepared powders indicates the powders are amorphous (inset Fig. 7a). The corresponding SAED pattern of calcined Y_2O_3 is presented in Fig. 7d. The SAED pattern contains multiple diffraction spots organized in rings, which demonstrates the polycrystallinity of the calcined powders. The diffraction rings are indexed to (2 1 1), (2 2 2), (4 0 0), (4 1 1), (3 3 2), (4 3 1), (4 4 0), (6 1 1), (6 2 2), (4 4 4), and (7 2 1) planes for cubic Y_2O_3 structure. The interplanar spacing (d_{hkl}) calculated from SAED patterns is consistent with the (d_{hkl}) values from the XRPD database (JCPDS: 01-073-1334).

4. Conclusions

Luminescent monodispersed $Y_2O_3:Eu^{3+}$ nanocrystalline spheres are obtained by a novel microwave assisted urea precipitation method followed by calcination of the particles at elevated temperatures. The microwave-assisted method is recognized as a surfactant and hazardous precursor free as well as quick and reproducible method. The as obtained particles with a $(Y,Eu)(OH)(CO_3)$ structure convert to Y_2O_3 at temperatures above 500 °C. Although the size of $(Y,Eu)(OH)(CO_3)$ particles decreases upon heat treatment and phase transformation, the spherical shape and monodispersity is preserved even at high calcination temperatures. The calcined particles with overall sizes less than ~100 nm have a polycrystalline structure with the crystallites of ~19 nm. The average crystallite size calculated with Scherrer and W–H equation methods are similar and consistent with TEM observations, which increases with the calcination temperature. The PL analyses of $Y_2O_3:Eu^{3+}$ nanophosphors show the strong red emission at 613 nm confirming the insertion of Eu^{3+} ions into the host matrix. Furthermore, the high R/O values support the variation of the local symmetry around Eu^{3+} in the cubic Y_2O_3 crystal structure and are dependent on the dopant concentration and independent on the calcination temperature. The PL intensity increases with the calcination temperature due to high crystallinity and with the Eu^{3+} concentration probably due to higher number PL active centers. The luminescence quenching commonly seen for similar nanocrystals using other methods has not been observed in our samples up to Eu^{3+} concentration of 13 mol% that reveals the improved quality of nanocrystals fabricated with the developed route. The red emission characteristics, morphological properties as spherical shape, monodispersity and the non-agglomeration, combined with potential low toxicity (being heavy-metal free) render these particles as promising biolabels and bio imaging probes.

Acknowledgments

The authors acknowledge partial support from the Swedish Research Council (VR-SRL 2013-6780). The authors also acknowledge valuable discussions with Dr. N. Krishna Chandar, KTH, Sweden.

Appendix A. Supplementary material

Supplementary data associated with this article can be found in the online version at [doi:10.1016/j.jlum.2015.08.059](https://doi.org/10.1016/j.jlum.2015.08.059).

References

- [1] G. Jia, H. You, Y. Song, Y. Huang, M. Yang, H. Zhang, *Inorg. Chem.* 49 (2010) 7721.
- [2] C.A. Traina, J. Schwartz, *Langmuir* 23 (2007) 9158.
- [3] T.S. Atabaev, J.H. Lee, D.W. Han, Y.H. Hwang, H.K. Kim, *J. Biomed. Mater. Res. – Part A* 100A (2012) 2287.
- [4] V. Kumar Rai, A. Pandey, R. Dey, *J. Appl. Phys.* 113 (2013) 083104.
- [5] P. Packiyaraj, P. Thangadurai, *J. Lumin.* 145 (2014) 997.
- [6] H.-Y. Xie, J.-G. Liang, Z.-L. Zhang, Y. Liu, Z.-K. He, D.-W. Pang, *Spectrochim. Acta Part A: Mol. Biomol. Spectrosc.* 60 (2004) 2527.
- [7] F. Pinaud, X. Michalet, L. a Bentolila, J.M. Tsay, S. Doose, J.J. Li, G. Iyer, S. Weiss, *Biomaterials* 27 (2006) 1679.
- [8] A. Pandey, M.K. Roy, A. Pandey, M. Zanella, R.A. Sperling, W.J. Parak, A. B. Samaddar, H.C. Verma, *IEEE Trans. Nanobiosci.* 8 (2009) 43.
- [9] D. Dosev, B. Guo, I.M. Kennedy, *J. Aerosol Sci.* 37 (2006) 402.
- [10] A. Pandey, V.K. Rai, *Appl. Phys. B* 109 (2012) 611.
- [11] V.K. Rai, R. Dey, K. Kumar, *Mater. Res. Bull.* 48 (2013) 2232.
- [12] W. Liu, Y. Wang, M. Zhang, Y. Zheng, *Mater. Lett.* 96 (2013) 42.
- [13] S. Zhong, J. Chen, S. Wang, Q. Liu, Y. Wang, S. Wang, *J. Alloy. Compd.* 493 (2010) 322.
- [14] C.A. Kodaira, A.V.S. Loureno, M.C.F.C. Felinto, E.M.R. Sanchez, F.J.O. Rios, L.A. O. Nunes, M. Gidlund, O.L. Malta, H.F. Brito, *J. Lumin.* 131 (2011) 727.
- [15] J. Zhang, Z. Tang, Z. Zhang, W. Fu, J. Wang, Y. Lin, *Mater. Sci. Eng. A* 334 (2002) 246.
- [16] Z. Yongqing, Y. Zihua, D. Shiwen, Q. Mande, Z. Jian, *Mater. Lett.* 57 (2003) 2901.
- [17] J. Dhanaraj, R. Jagannathan, T.R.N. Kutty, C.-H. Lu, *J. Phys. Chem. B* 105 (2001) 11098.
- [18] S. Mukherjee, V. Sudarsan, P.U. Sastry, A.K. Patra, A.K. Tyagi, *J. Lumin.* 145 (2014) 318.
- [19] M.K. Devaraju, S. Yin, T. Sato, *Eur. J. Inorg. Chem.* 2009 (2009) 4441.
- [20] J. Yang, Z. Qian, D. Kong, X. Liu, J. Lin, *Cryst. Growth Des.* 7 (2007) 730.
- [21] T. Hirai, Y. Asada, I. Komasa, J. Colloid Interface Sci. 276 (2004) 339.
- [22] T. Yan, D. Zhang, L. Shi, H. Yang, H. Mai, J. Fang, *Mater. Chem. Phys.* 117 (2009) 234.
- [23] N. Venkatchalam, T. Yamano, E. Hemmer, H. Hyodo, H. Kishimoto, K. Soga, *J. Am. Ceram. Soc.* 96 (2013) 2759.
- [24] Y.-P. Fu, C.-H. Lin, *J. Alloy. Compd.* 389 (2005) 165.
- [25] A. Vadivel Murugan, A.K. Viswanath, V. Ravi, B.A. Kakade, V. Saaminathan, *Appl. Phys. Lett.* 89 (2006) 123120.
- [26] A. Malek Khachatourian, F. Golestani-Fard, H. Sarpoolaky, C. Vogt, M.S. Toprak, *Ceram. Int.* 41 (2015) 2006.
- [27] B. Antic, A. Kremenović, M. Vucinic-Vasic, Z. Dohcevic-Mitrovic, A.S. Nikolic, M. Gruden-Pavlovic, B. Jančar, A. Meden, *Mater. Chem. Phys.* 122 (2010) 386.
- [28] L.E.A. Harold, P. Klug, *X-Ray Diffraction Procedures: For Polycrystalline and Amorphous Materials*, second ed., John Wiley & Sons, New York, 1974.
- [29] C. de Mayrinck, D.P. Santos, S.J.L. Ribeiro, M.A. Schiavon, J.L. Ferrari, *Ceram. Int.* 40 (2014) 15965.
- [30] L.S. Chi, R.S. Liu, B.J. Lee, *J. Electrochem. Soc.* 152 (2005) J93.
- [31] Y. Huang, D. Jiang, J. Zhang, Q. Lin, Z. Huang, *Ceram. Int.* 37 (2011) 3523.
- [32] S. Som, S.K. Sharma, T. Shripathi, *J. Fluoresc.* 23 (2013) 439.
- [33] R.H. Krishna, B.M. Nagabhushana, H. Nagabhushana, N.S. Murthy, S.C. Sharma, C. Shivakumara, R.P.S. Chakradhar, *J. Phys. Chem. C* 117 (2013) 1915.
- [34] A. Boukerika, L. Guerbous, *J. Lumin.* 145 (2014) 148.
- [35] Y. Xiao, D. Wu, Y. Jiang, N. Liu, J. Liu, K. Jiang, *J. Alloy. Compd.* 509 (2011) 5755.
- [36] M.L. Pang, J. Lin, Z.Y. Cheng, J. Fu, R.B. Xing, S.B. Wang, *J. Mater. Sci. Eng. B: Solid-State Mater. Adv. Technol.* 100 (2003) 124.
- [37] S. Som, M. Chowdhury, S.K. Sharma, *J. Mater. Sci.* 49 (2013) 858.
- [38] H.S. Yoo, H.S. Jang, W. Bin Im, J.H. Kang, D.Y. Jeon, *J. Mater. Res.* 22 (2011) 2017.
- [39] J. Chen, F. Gu, W. Shao, C. Li, *Phys. E: Low-Dimensional Syst. Nanostruct.* 41 (2008) 304.
- [40] N. Vu, T. Kim Anh, G.-C. Yi, W. Strek, *J. Lumin.* 122–123 (2007) 776.
- [41] J. Silver, M.I. Martinez-Rubio, T.G. Ireland, G.R. Fern, R. Withnall, *J. Phys. Chem. B* 105 (2001) 9107.
- [42] J. Blanusa, N. Jovic, T. Dzomic, B. Antic, A. Kremenovic, M. Mitric, V. Spasojevic, *Opt. Mater. (Amst)* 30 (2008) 1153.
- [43] B. Antic, J. Rogan, A. Kremenovic, A.S. Nikolic, M. Vucinic-Vasic, D.K. Bozanic, G.F. Goya, P.H. Colomban, *Nanotechnology* 21 (2010) 245702.
- [44] G. Wakefield, E. Holland, P.J. Dobson, J.L. Hutchison, *Adv. Mater.* 13 (2001) 1557.
- [45] D. Wang, Q. Yin, Y. Li, M. Wang, *J. Lumin.* 97 (2002) 1.
- [46] M.S. Kwon, H.L. Park, T.W. Kim, Y. Huh, W. Choi, J.Y. Lee, *Met. Mater. Int.* 12 (2006) 263.
- [47] L. Robindro Singh, R.S. Ningthoujam, V. Sudarsan, I. Srivastava, S. Dorendrajit Singh, G.K. Dey, S.K. Kulshreshtha, *Nanotechnology* 19 (2008) 055201.
- [48] X. Hou, S. Zhou, Y. Li, W. Li, *J. Alloy. Compd.* 494 (2010) 382.
- [49] T.L. Phan, M.H. Phan, N. Vu, T.K. Anh, S.C. Yu, *Phys. Status Solidi Appl. Res.* 201 (2004) 2170.
- [50] W.-N. Wang, W. Widiyastuti, T. Ogi, I.W. Lenggoro, K. Okuyama, *Chem. Mater.* 19 (2007) 1723.